Nanoscale

Accepted Manuscript

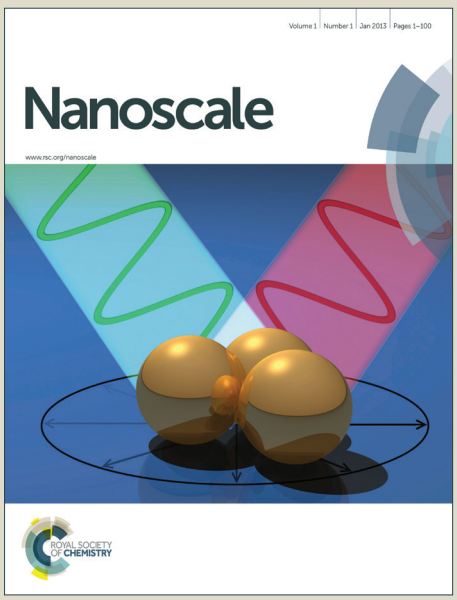

ROYAL SOCIETY OF CHEMISTRY

www.rsc.org/nanoscale

Nanoscale

COMMUNICATION

Dependence of Young's Modulus on the Sodium Content within the Structural Tunnels of a One-Dimensional Na-Ion Battery Cathode

Received 00th January 20xx,
Accepted 00th January 20xx

DOI: 10.1039/x0xx00000x

www.rsc.org/

M. Maksud,[a] N. K. R. Palapati,[a] B. Byles,[b] E. Pomerantseva,[b] Y.Liu,[c] and A. Subramanian[a]

We report on the Young's modulus (YM) of single-crystalline $Na_4Mn_9O_{18}$ (or $Na_{0.44}MnO_2$) nanowires (NWs), which have shown promise as reversible sodium-ion (Na^+) intercalation cathodes with high capacity and excellent cyclability. In addition, acid treatment of this material yielded proton stabilized $Na_{0.44-y}MnO_2$ (y ~ 0.23) NWs with a 74% increase in the YM. The tight correlation between YM and ionic content within the crystalline tunnels is particularly significant, since it points to the strong dependence of elastic properties on state-of-charge (SOC) within battery materials.

In electrochemical energy storage systems involving reversible insertion / extraction of inorganic ions, such as sodium and lithium,[1] one of the key requirements for improving the cycle life and rate capability of a battery electrode is its ability to reversibly host the "guest" ions at high capacities and high rates without structural and mechanical degradation.[2-4] Mechanical degradation causes undesirable effects, which include electrode fracture, delamination and higher impedances for the transport of charge carriers, eventually resulting in battery failure.[5-10]

As a result, computational models have been developed to estimate the evolution of both, stress fields and fracture as a function of ionic diffusion inside battery electrodes.[5-10] A knowledge of the elastic properties of the material, particularly its Young's Modulus, is an essential input to these computational models. For instance, YM was a key parameter in the development of particle size-dependent fracture mechanics behaviour in $Li_xMn_2O_4$ and $LiFePO_4$ electrode systems.[5,6] Ref. [10] has also highlighted the strong correlation between the YM of lithium manganese oxides and the resultant lithiation-induced stress fields, with a discussion that "its [i.e., YM's] precise measurement is technically significant".

Past measurements on the elastic properties of battery materials have focused predominantly on alloying anodes, such as silicon[11] This is due to the extremely large volume changes (up to 400% in Si) and mechanical strains observed during the electrochemical charging of these materials. On the other hand, there are only isolated measurements on the elastic properties of battery cathode materials even though mechanical degradation has contributed to the failure of these materials as well.[5,7] In the case of manganese oxides, past YM measurements have involved only its lithium-containing spinel-phase. Different measurement methods and sample preparation techniques have yielded different YM values, which have varied over a wide range from 10GPa to hundreds of GPa. [13,14] For example, an elastic modulus of 10GPa was reported when a vibrating-reed technique was used with gold coated, polycrystalline bars obtained from cold-pressed $LiMn_2O_4$ powders.[13] Another report has employed X-ray diffraction techniques on bulk-scale powders of $LiMn_2O_4$ nanorods to obtain a Young's modulus of 143GPa.[14] Our approach, which will be described below, represents an improvement in that it provides accurate insights into the intrinsic YM of the electrode crystal without introducing any ensemble averaging (in terms of grain orientations, particle size, shape, and / or inter-particle interfaces) or coating effects, which have been associated with past measurements. Specifically, we employ an AFM-based, three-point bending technique[15-18] on single NW crystals to accurately quantify the intrinsic YM of the material system. Furthermore, we present new insights into the changes in elasticity of the crystal when its ionic content is modified, pointing to the SOC dependence of material elasticity during its electrochemical cycling. This is important since the models, which are in use today for predicting fracture in battery electrodes, always assume a constant YM value due to a lack of experimental data related to its dependence on ion concentration.[5-7]

Our choice of a Na-ion intercalation material is motivated by the emerging interest in this ionic system due to the low-cost and abundant availability of sodium as compared to lithium. [19,20] Furthermore, intercalation-induced volume changes and fracture is a bigger issue in Na-ion battery electrodes due to the larger ion

[a] Department of Mechanical and Nuclear Engineering, Virginia Commonwealth University, Richmond, VA 23284, USA. Email: asubramanian@vcu.edu.
[b] Department of Materials Science and Engineering, Drexel University, Philadelphia, PA 19104, USA.
[c] Department of Materials Science and Engineering, North Carolina State University, Raleigh, NC 27606, USA.
See DOI: 10.1039/x0xx00000x

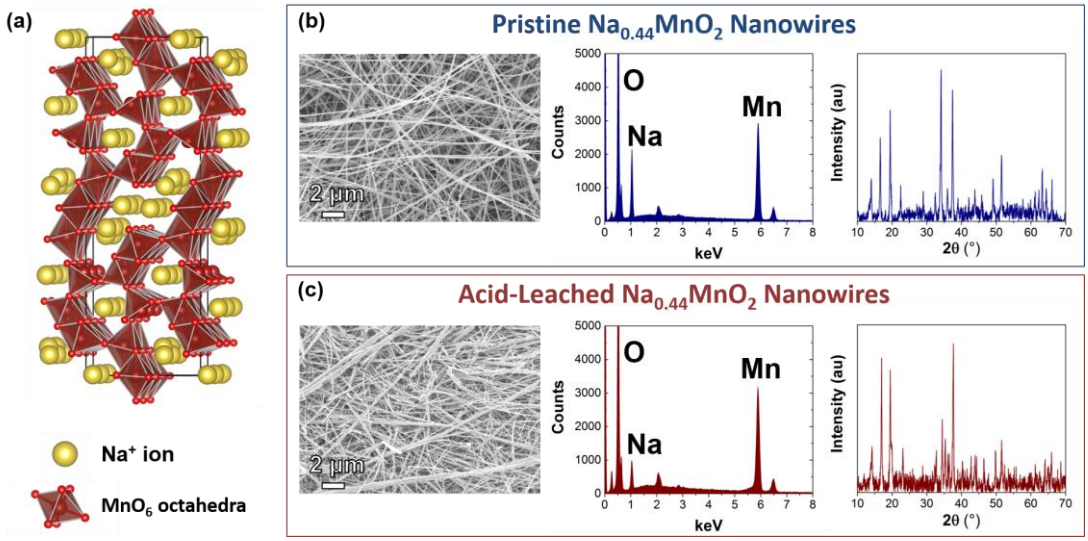

Figure 1. (a) Schematic representation of the crystal structure of $Na_4Mn_9O_{18}$ nanowires with two types of the structural tunnels occupied by Na^+ ions. Morphology, composition and structure characterization of (b) pristine and (c) acid-leached $Na_4Mn_9O_{18}$ nanowires (from left to right: SEM image, EDX spectrum and XRD pattern of the respective material).

radius of Na^+ as compared Li^+ (1.06Å vs. 0.76Å).[20] Thus, an accurate measurement of the YM of Na-ion electrodes is especially critical to study their mechanical stability and to thereby, improve the cycle-life / sustainability of these systems.

This effort has focused on one-dimensional (NW-based) orthorhombic crystals of sodium-containing manganese oxide, $Na_{0.44}MnO_2$ or $Na_4Mn_9O_{18}$ (Figure 1). These nanowires were synthesized by hydrothermally treating Mn_2O_3 or Mn_3O_4 powder in 6 M aqueous NaOH solution. [2,3,21,22] More specifically, 0.08 g of Mn_2O_3 powder was dispersed in 6 M NaOH solution under vigorous stirring. The suspension was then placed in a 23 ml, Teflon-lined autoclave (Parr Instrument Company) and heated at 220°C for 6 days. After the hydrothermal treatment, the synthesized $Na_4Mn_9O_{18}$ nanowires were thoroughly washed with the deionized water and dried at 100°C for 12 hours in vacuum. The crystal structure of this material is built by MnO_6 octahedra and MnO_5 square pyramids sharing corners and edges in order to form large-sized tunnels around the sodium ions (Figure 1a). As shown in Figure 1(a), the Mn-O framework envelops two types of tunnels that run along the longitudinal or *c*-axis: (1) larger sized, z-shaped tunnels, and (2) smaller, pentagonal tunnels. Both types of tunnels are stabilized by sodium ions and the larger ones present crystallographic sites for reversible Na^+ intercalation (Figure 1a). Hence, this material has yielded results, which have established its performance as a high capacity cathode for Na-ion batteries with excellent cyclability.[23-27] In the nanowire form, $Na_4Mn_9O_{18}$ phase shows high capacities up to 128 mAh/g and stable performance during extended cycling in a Na-ion system. [2,3]

We have employed acid leaching (AL), which is a chemical technique, to mimic the electrochemical extraction of sodium ions from the as-synthesized or pristine $Na_{0.44}MnO_2$ NWs and then, studied its impact on the material YM. Following a previous report,[28] we used concentrated nitric acid at room temperature for this chemical extraction of sodium ions from the pristine NWs. In order to achieve this, the pristine NWs were kept in HNO_3 for 24 hours under constant stirring. The NWs were then repeatedly washed with deionized water until a neutral pH was achieved, and dried at 100°C for 12 hours in vacuum. A key advantage with this method is that it can be applied directly with the electroactive material in isolation, as opposed to electrochemical cycling where the electroactive material is typically mixed with conductive carbon and a polymer binder to form the functional electrode. Thus, our chemical method obviates the need for post-cycling separation of electroactive material from the rest of the electrode in order to measure its intrinsic composition dependent parameters (such as its YM). Manganese oxides are especially attractive for such an investigation as they do not dissolve even in strong oxidizing acids.

Previous studies have shown that this AL of manganese oxides with the general formula of A_xMnO_2 (where A is alkaline or alkali-earth element) involves two parallel material transformations, both of which also occur in the electrochemical charging of these materials. First, during AL, the A ions are extracted from the crystal structure of the material and this process is often accompanied by an ion exchange with protons. This is similar to the electrochemical charging process, which involves the potential-dependent extraction of A ions. In addition, ion exchanged protons have also been found to electrochemically intercalate into the electrode material from the trace amounts of HF acid present in hexafluorophosphate based electrolytes.[29-33] In fact, protons, which also occur naturally in electrolytic manganese dioxide (EMD), have been hypothesized to play an important role in controlling charge storage properties of manganese oxides, as will be discussed later.

The second material transformation during AL involves the disproportionation of Mn^{3+} ions into Mn^{4+} (remaining in the solid

material) and Mn^{2+} (dissolving in the acid). Therefore, the average Mn oxidation state in acid-leached manganese oxides is higher than in pristine materials.[28,34-36] An increase in transition metal oxidation state occurs during electrochemical extraction of charge carrying ions as well though, in this case, it has its origins in vacancies created by the extraction of ions. Thus, acid-leached manganese oxides, which are used in our effort, lend themselves well to obtain insights into the SOC-dependent material properties of their electrochemical counterparts. This argument is supported by a past study of chemical *vs.* electrochemical extraction of lithium ions for $Li_{1.10}Mn_{1.90}O_4$ spinel material. This report has established that intermediate de-intercalated products prepared during the chemical extraction process (by acid treatment) are similar to those prepared by the electrochemical way in non-aqueous electrolytes. [37]

The morphology and chemical composition of both, the pristine and acid-leached nanowires were investigated using a Zeiss Supra 50VP (Germany) scanning electron microscope (SEM), which was equipped with an energy dispersive X-ray spectroscopy (EDS) attachment. In our case, the acid treatment was found to not affect the nanowire morphology of the material (Figure 1, b-c). According to EDX spectroscopy data (Figure 1, b-c), the Na/Mn ratio dropped from 0.44 in pristine $Na_4Mn_9O_{18}$ nanowires to 0.21 in the acid-leached material. Thus, we obtained proton-stabilized $Na_{0.44-y}MnO_2$ (y ~ 0.23) NWs, or simply AL NWs, as the end-product of our acid treatment process. This corresponds well with the final composition achieved previously for electrochemically charged $Na_4Mn_9O_{18}$ nanowires, which showed stable cycling in the composition range of $0.22 < x < 0.66$, where x is Na content in Na_xMnO_2.[3] This agreement in composition further reaffirms the feasibility of the acid leaching process to mimic electrochemical extraction of ions. Phase identification was carried out by X-ray powder diffraction (XRD) experiments on a Rigaku SmartLab powder diffractometer (Japan) with Cu Kα radiation (step size 0.02° in the range of $10° < 2\theta < 70°$). XRD patterns of the pristine and acid-leached $Na_4Mn_9O_{18}$ nanowires (Figure 1, b-c) agree with the previously published results, indicating shrinkage of the unit cell due to acid treatment. The decrease in unit cell volume was attributed to the extraction of large Na^+ ions from structural tunnels and to the increase in oxidation state of manganese ions (0.645 Å ionic radius for Mn^{3+} in high-spin configuration vs. 0.53 Å for Mn^{4+}). Such modifications in material composition and structure, which are caused by the acid leaching process, result in a substantial change of the Young's Modulus, as will be shown later.

While a change in ionic content is verified by the EDX data in Figure 1, the argument that the acid-leached NWs are single-phase, tunnel-crystalline materials, which retain their original morphology, is further confirmed from the selected area electron diffraction (SAED) and high-resolution transmission electron microscopy (HR-TEM) data. For these experiments, the nanowires were suspended in ethanol using ultrasonication, and then dispersed onto carbon supported copper TEM grids. The TEM grids were mounted on to a Gatan double-tilt holder, which was inserted into a JEOL 2010F field-emission TEM operating at 200 kV. Gatan CCD camera and Digital Micrograph software were used for recording and analyzing images. These results, which are shown in Figure 2, confirm that both, the pristine and acid-leached nanowires are single-crystalline and single-phase materials. Furthermore, the presented TEM data indicate that the [001] direction of the unit cell (i.e., the 1-D structural tunnels) is oriented along the longitudinal axis of the NWs.

The YM of these NW material systems is extracted from three-point bending tests, which are performed using contact mode atomic-force microscopy (AFM).[15-18] In order to perform these three-point bending tests, individual NWs are integrated into doubly-clamped nanomechanical beams on the surface of silicon chips. The single NW device architecture is shown in Figure 3. In this device, a single NW bridges a pair of gold nanoelectrodes and remains suspended in air in the inter-electrode region. The electrode gaps are fixed either at 400nm or 800nm in different design variants and typically include a lithography induced bias in the actual structures.

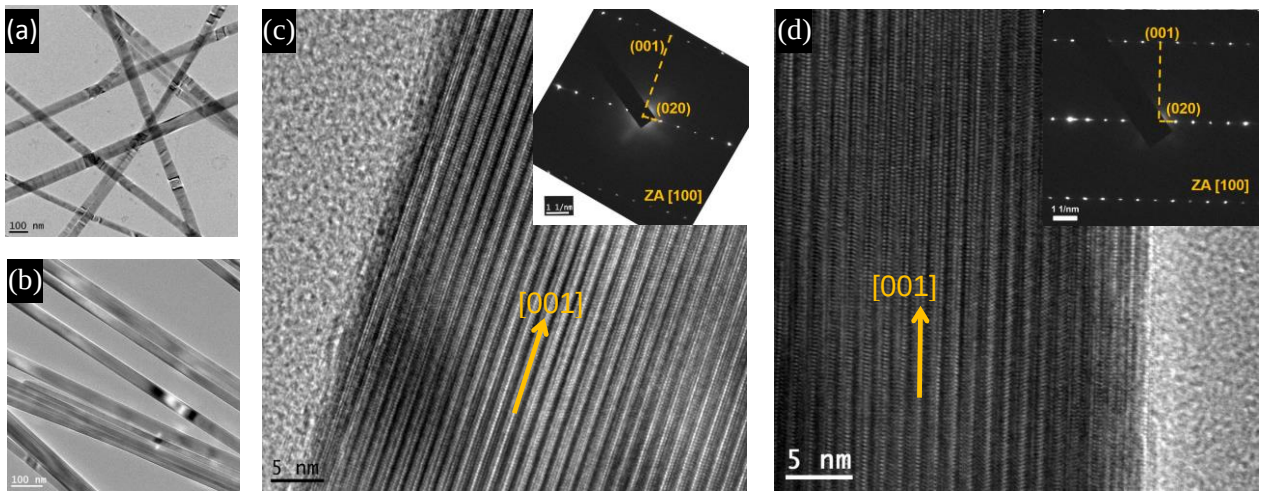

Figure 2. (a-b) TEM images of pristine and acid-leached $Na_4Mn_9O_{18}$ NWs, respectively. The scale bars in these panels measure 100nm. (c) HR-TEM image of a pristine NW with its SAED pattern (obtained from a [100] zone-axis) in the inset. (d) HR-TEM of an acid-leached NW with its SAED pattern in the inset. Scale bars in panels 'c' and 'd' measure 5nm. These images confirm that both, the pristine and acid-leached NWs are single crystalline and single-phase materials.

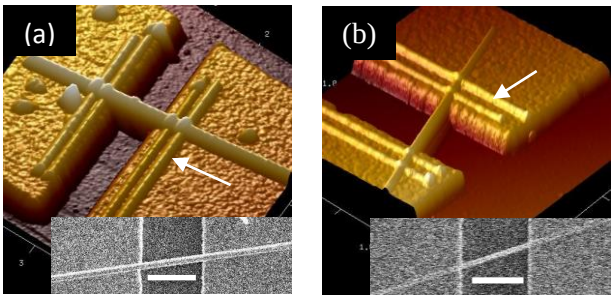

Figure 3. A 3D plot of the (a) pristine and (b) acid-leached $Na_4Mn_9O_{18}$ nanowires, which were acquired using tapping mode AFM. The white arrows point at EBID clamping. SEM images of these NWs, taken prior to EBID clamping, are shown in the insets. The SEM scale bar in both panels measures 600 nm.

The devices are realized using an on-chip nanofabrication approach, which uses a combination of top-down silicon nanomachining and bottom-up dielectrophoretic (DEP) nanoassembly techniques. This nanoassembly-enabled fabrication approach, which has been presented in detail in our past reports,[38-40] involves the following steps. A silicon chip, which measures 4mm by 6mm and has an insulating layer of 100nm thick nitride film on its top-side, serves as the starting substrate. We first fabricate gold nanoelectrode pairs on top of this substrate using electron beam lithography and metal lift-off. The gold electrodes are deposited with a film thickness of 100nm and employ an underlying, 15nm layer of chromium to promote adhesion to the nitride layer. Next, the silicon chips are placed in a reservoir containing a suspension of NWs in ethanol and an AC electric field is applied across the gold nanoelectrode pairs. The applied electric field polarizes the NWs in the suspension and the resulting DEP force attracts the NWs towards the electric field maxima, resulting in their deposition across the electrodes. Through a suitable selection of AC voltage, its frequency and deposition ti this DEP process yields the assembly of single NWs, which ar suspended in air across the gold electrode pairs (Figure 3).[38] Finall the NWs are further clamped onto the gold electrodes using top-sid metallization, which is achieved using electron beam induce deposition (EBID) of platinum. This insures that the NWs are securely anchored in a doubly-clamped beam configuration without slippag at the contacts during the three-point bending tests (Figure 3).

The three-point bending test was performed using a VEECO Icon AFM. Silicon nitride cantilevers with a spring constant in the 3-13N/m range were used in these experiments. This experiment, which is shown schematically in Figure 4(a) and is used to obtain the YM fro force versus displacement (F-d) curves of the NW beam, involves th following steps.[16-18] The AFM tip is positioned on top of the N sample at its suspended mid-length and the sample, which is controlled in height by the z-piezo of the sample stage, is pushed against the tip. At its starting point, the AFM tip and the stage a separated by a few tens of nanometers in distance. As the NW sample comes in contact with the AFM tip, the tip is deflected upwards. During this process, the deflection of the AFM tip (Z_{tip}) an the movement of the stage (Z_{piezo}) are monitored. The deflection o the NW beam (Z_{NW}) at any given stage position is computed as:

$$Z_{NW} = Z_{piezo} - Z_{tip} \quad (1)$$

The force exerted by the AFM tip on the NW (F_{NW}), which is equal t the mechanical restoring force of the tip (F_{tip}), is given as:

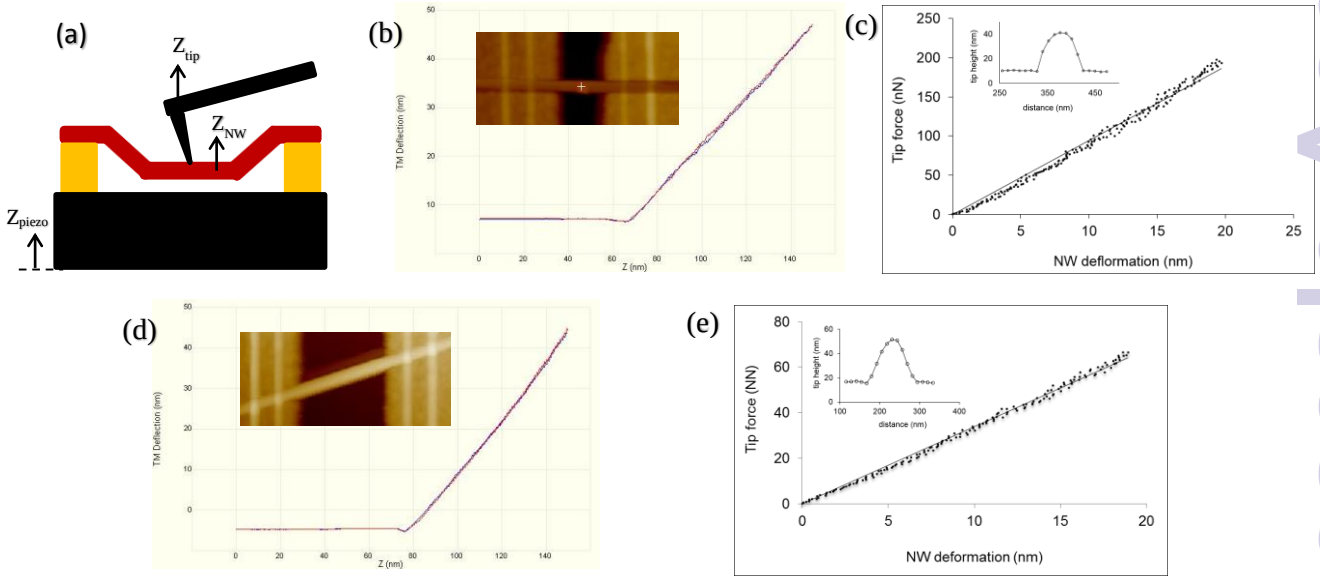

Figure 4. (a) A schematic of the AFM-based three-point bending test showing the tip, NW and stage (piezo) displacement variables. (b) A contact-mode AFM plot from a $Na_{0.44}MnO_2$ NW showing the tip deflection as a function of the AFM piezo displacement. The trace (blue) and re-trace (red) curves representing the engagement of the tip with the NW sample is shown in this plot. The NW AFM image is shown in inset. (c) The force vs. displacement plot of the NW sample, which is extracted from the contact-mode plot of panel 'b', is shown here. Here, the black dots represent the experimental data while the solid line denotes its linear fit. From the slope of this linear fit (i.e., the NW stiffness), the YM of this 31nm diameter NW is calculated as 79 GPa. The height trace of the NW, which is used to calculate its diameter, is shown in the inset. (d) The tip deflection vs. AFM piezo displacement plot for an AL NW with its AFM image in the inset. (e) The force vs. deflection plot of the NW of panel 'd'. The NW height trace is shown in the inset. The YM of this 35nm diameter NW was calculated as 147.1 GPa.

$$F_{NW} = F_{tip} = k_{tip} Z_{tip} \quad (2)$$

where k_{tip} represents the mechanical stiffness of the AFM cantilever, and is computed from Sader's resonance damping model.[41] In these measurements, the raw tip deflection data is in the form of photodetector voltage signals. This is converted into the equivalent tip deflection values (in nm) by a calibration step where the tip is pushed against a rigid surface (gold electrode).

The AFM three-point bending test results are shown for a representative $Na_4Mn_9O_{18}$ NW device in Figure 4(b-c). The tip deflection *vs.* stage position data is shown in panel 'b' and the extracted F-d plot is shown in panel 'c'. Figure 4(c) assumes a linear profile since the NW deforms in a pure bending mode in this regime where the maximum deflection is on the order of its thickness.[16-18] The slope of this F-d plot indicates the nanomechanical stiffness (k_{NW}) of the NW beam and is related to its Young's Modulus (E) by the following equation: [16-18]

$$k_{NW} = {}^{192EI}/_{l_{NW}^3} \quad (3)$$

where I ($= \pi r^4/4$), r and l_{NW} denote the NW moment of inertia, radius and suspended length, respectively. The NW diameter is estimated from its height trace plot (inset of Figure 4(b)), which is acquired from a separate tapping mode AFM scan, to be 31nm for this representative NW. Also, the NW length is extracted from its SEM image to be 408nm. Using the F-d slope, NW radius and diameter values in Equation (3), we compute the YM of this NW to be 79 GPa.

The YM values of 6 pristine $Na_4Mn_9O_{18}$ NW samples is plotted as a function of their diameter in Figure 5. The average YM value of these 6 NW beams, which ranged between 26nm to 78nm in diameter and between 371nm to 828nm in length, was found to be 84.3 $\pm$ 9.1 GPa (the interval denotes the 95% confidence interval). An interesting aspect that emerges from the presented data is its diameter independence. This confirms that the NWs have a uniform crystal structure across their cross-section without any surface effects such as bond-length contractions,[42] surface relaxation[43] or amorphous coatings.[18] In the case of other NW material systems such as zinc oxide and cobalt oxide, these surface effects were reported to cause an outsized influence on smaller diameter nanowires and have resulted in an increasing YM with decreasing NW size.[18,42,43] This work represents the first measurement of the YM of the $Na_4Mn_9O_{18}$ material system, which in a nanostructured or nanowire morphology is one of the promising candidates under investigation for high capacity Na-ion battery cathodes.

As a next step, we assembled acid-leached (AL) $Na_4Mn_9O_{18}$ NW beams (Figure 3(b)) and measured their YM. For the representative AL NW shown in Figure 4(d-e), which had a diameter and length of 35nm and 843nm, respectively, the YM was extracted to be 147.1 GPa. Furthermore, the YM values obtained from 7 different AL-$Na_4Mn_9O_{18}$ NW samples is plotted in Figure 4 as a function of their diameter. From this data, the average YM value for the acid-leached NWs was observed to be 146.4 ± 12.4 GPa. This represents a 74% increase from the observed average value of 84.3 ± 9.1 GPa for the pristine, $Na_4Mn_9O_{18}$ material system.

We attribute this difference in the observed YM values for pristine and acid-leached nanowires to three factors, each of which arises from the difference in ionic content inside the structural tunnels of these two materials. First, the pristine material has 0.44 sodium ions per MnO_2 while the acid-leached counterpart has only 0.21 Na^+ ions per MnO_2 (EDX analysis, Figure 1 b-c). The remaining 0.23 sodium sites inside the crystal tunnels of the AL NWs are partially exchanged with protons, as discussed previously. The higher Na^+ content within the tunnels leads to a larger unit cell volume in the case of the pristine material as compared to its acid-leached counterpart.[44] It is important to note that the presence of protons is not expected to significantly affect the tunnel size due to their extremely small radius. Thus, the Mn-O bonds are weaker within the pristine material due to the larger unit cell, and thereby, result in its elastic softening. Our argument is supported by previous results where Rietveld analysis was performed on XRD data to obtain the unit cell parameters for pristine and AL $Na_4Mn_9O_{18}$ phases.[28] Here, the *a* and *c* lattice parameters remained nearly unchanged. On the other hand, the *b* parameter was observed to decrease by 4% (from 26.236(4) Å to 25.22(1) Å) when the Na^+ content decreased from 0.44 to 0.11.

The second factor, which arises from ionic content induced changes in the AL material and plays a role in its higher YM, relates to the Mn^{3+} ion disproportionation process.[28] This conversion of Mn^{3+} to Mn^{4+} during the acid treatment process, accompanied by the associated dissolution of the Mn^{2+} ion, will reduce the content of these larger Mn^{3+} Jahn-Teller ions[45] in the AL NWs. This alleviation of Jahn-Teller distortions within the MnO_6 octahedra, combined with the smaller size of the Mn^{4+} ions, also contributes to the increase in the YM of AL NWs.

The third factor in the increase of YM relates to the incorporation of protons into the tunnels during the AL process. It has been shown that these protons form hydroxyl groups by bonding with oxygen anions in the Mn-O framework. These hydroxyl groups are believed to be located near the manganese vacancies within the crystal

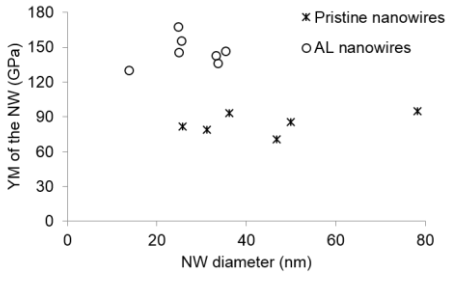

Figure 5. A comparison of the YM values, which were obtained from 6 pristine and 7 AL NW samples, respectively. The mean YM value was obtained as 84.3 $\pm$ 9.1 GPa and 146.4 $\pm$ 12.4 GPa for the pristine and AL NWs, respectively. The intervals specified for the means represent a 95% confidence level.

lattice[34,46] in such a manner that they stabilize the crystal structure of the material during reversible, ion intercalation. We conclude that these additional bonds and the resultant stabilization of the crystal due to the incorporation of protons is also a contributing factor to the observed increase in YM. This argument is further supported by the observation of improved capacity retention during electrochemical lithium cycling of layered $LiMn_2O_4$ spinels, which was directly attributed to proton insertion-induced structural stabilization.[32]

It is important to note that, as discussed in detail earlier, a decrease in content of charge carrying ions and an increase in the transition metal oxidation state are also characteristic of these intercalation-based oxide cathodes during their respective charge cycles in batteries. While partial proton substitution of the charge carrying ions is not always characteristic of electrochemical charge processes in other battery materials, proton incorporation has indeed been observed in manganese oxides when they are electrochemically charged using hexafluorophosphate-based electrolytes. Furthermore, electrolytic manganese dioxides (EMD) have been found to contain naturally occurring protons. Therefore, we believe that our acid-leached material is representative of its electrochemically charged counterpart (as similarly reported with the acid leached *vs.* electrochemical extraction of lithium ions from $Li_{1.10}Mn_{1.90}O_4$ spinel material),[37] and provides accurate insights into the modulation in YM with a variation in SOC for this material system. Even with the much better understood lithium-ion system, this dependence of YM on ionic concentration in manganese oxides has only been computationally modeled and has not been experimentally verified. For instance, Lee et. al. have presented molecular dynamics simulations to show that the YM of a spinel Li_xMnO_2 varies by up to 18% depending on its Li content.[8] Thus, our effort presents the first measurements of ionic-content dependent YM values within tunnel crystal manganese oxides, which are suitable for any metal-ion intercalation-based electrochemical system (i.e., Li as well as Na).

Conclusions

We have presented an experimental approach for measuring the YM of sodium manganese oxide-based, one-dimensional crystals at a single particle-level. The measured average YM of 84.3 GPa was found to increase to 146.4 GPa when the Na/Mn ratio was reduced by 0.23 using the acid leaching method, which mimics the charging process in electrochemically cycled cells. The increase in YM is attributed to a strengthening of Mn-O bonds, reduction of Jahn-Teller distortions and protonic stabilization, each of which has its origins in the changes in ionic content within the acid-leached crystal. These results point to the substantive dependence of elastic properties on the intercalation ion content in manganese oxide-based, tunnel crystal intercalation cathodes. These concentration dependent properties will play a significant role in the mechanical stability and fracture behaviour of this family of materials, which is a promising candidate for high-capacity sodium ion battery cathodes. The measured data is especially important in context of sodium ion batteries due to the large size of charging carrying ions in these systems. The capabilities of this reported measurement approach when combined with other in-situ techniques for investigating volumetric and structural changes in battery electrodes, will fully elucidate the inactivation mechanism in battery electrodes. This information will substantially advance our understanding of a wide variety of new material systems, which are currently being investigated for use in next generation battery and supercapacitor applications.

Acknowledgements

This work was partly supported by the National Science Foundation under Grant Nos. 1266438 and 1453966. EP also acknowledges the support from Drexel University start-up funds. The SEM and AFM imaging were performed at the VCU Nanomaterials Characterization Core (NCC) Facility. EP and BS are thankful to the Centralized Research Facility of Drexel University for use of XRD and SEM. We would also like to acknowledge the assistance of Dr. Indika Arachchige and Richard J. Esteves with preliminary TEM imaging of the NW crystals. This work was performed, in part, at the Sandia-Los Alamos Center for Integrated Nanotechnologies (CINT), a U.S. Department of Energy, Office of Basic Energy Sciences user facility. The chip nanofabrication activities were performed at CINT under the user proposal U2014A0084. Sandia National Laboratories is a multi-program laboratory operated by Sandia Corporation, a wholly owned subsidiary of Lockheed Martin company, for the U.S. Department of Energy's National Nuclear Security Administration under contract DE-AC04-94AL85000.

Notes and references

1 M. Armand and J.-M. Tarascon, *Nature*, 2008, **451**, 652.
2 Y. Cao, L. Xiao, W. Wang, D. Choi, Z. Nie, J. Yu, L. V. Saraf, Z. Yang, J. Liu, *Advanced Materials*, 2011, **23**, 3155.
3 E. Hosono, T. Saito, J. Hoshino,M. Okubo, Y. Saito, D. Nishi, Hamane, T. Kudo and H. Zhou, *Journal of Power Sources*, 2012, **217**, 43.
4 P. Arora, R. E. White and M. Doyle, *Journal of the Electrochemical Society*, 1998, **145**, 3647.
5 W. H. Woodford, Y.-M. Chiang and W. C. Carter, *Journal of the Electrochemical Society*, 2010, **157**, A1052.
6 Y. Hu, H. Zhao and Z. Suo, *Journal of Materials Research*, 2010, **25**, 1007.
7 H. Gabrisch, J. Wilcox and M. M. Doeff, *Journal of the Electrochemical Society*, 2008, **11**, A25.
8 S. Lee, J. Park, A. M. Sastry and W. Lu, *Journal of the Electrochemical Society*, 2013, **160**, A968.
9 J. Christensen and J. Newman, *Journal of the Electrochemical Society*, 2006, **153**, A1019.
10 J. Park, W. Lu and A. M. Sastry, *Journal of the Electrochemical Society*, 2011, **158**, A201.
11 H. Lee, W. Shin, J. W. Choi and J. Y. Park, *Journal of Physics D: Applied Physics*, 2012, **45**, 275301.
12 B. Hertzberg, J. Benson and G. Yushin, *Electrochemistry Communications*, 2011, **13**, 818.
13 A. Sugiyama, T. Tamura and H. Yamauchi, *Journal of Physics: Condensed Matter*, 1995, **7**, 9755.
14 Y. Lin, Y. Yang, H. Ma, Y. Cui and W. L. Mao, *The Journal of Physical Chemistry C*, 2011, **115**, 9844.

15 G. Pennelli, M. Totaro and A. Nannini, *ACS Nano*, 2012, **6**, 10727.
16 H. Kim, U. S. Jung, S. I. Kim, D. Yoon, H. Cheong, C. W. Lee and S. W. Lee, *Current Applied Physics*, 2014, **14**, 166.
17 Q. Xiong, N. Duarte, S. Tadigadapa and P. C. Eklund, *Nano Letters*, 2006, **6**, 1904.
18 B. Varghese, Y. Zhang, L. Dai, V. B. C. Tan, C. T. Lim and C.-H. Sow, *Nano Letters*, 2008, **8**, 3226.
19 V. Palomares, P. Serras, I. Villaluenga, K. B. Hueso, J. Carretero-Gonzalez and T. Rojo, *Energy and Environmental Science*, 2012, **5**, 5884.
20 M. D. Slater, D. Kim, E. Lee and C. S. Johnson, *Advanced Functional Materials*, 2013, **23**, 947.
21 E. Hosono, H. Matsuda, I. Honma, S. Fujihara, M. Ichihara and H. Zhou, *Journal of Power Sources*, 2008, **182**, 349.
22 Y. Li and Y. Wu, *Nano Research*, 2009, **2**, 54.
23 F. Sauvage, L. Laffont, J.-M. Tarascon and E. Baudrin, *Inorganic Chemistry*, 2007, **46**, 3289.
24 X. Zhou, R. K. Guduru and P. Mohanty, *Journal of Materials Chemistry A*, 2013, **1**, 2757.
25 L. Zhao, J. Ni, H. Wang and L. Gao, *RSC Advances*, 2013, **3**, 6650.
26 M. Xu, Y. Niu, C. Chen, J. Song, S. Bao and C.M. Li, *RSC Advances*, 2014, **4**, 38140.
27 P. Zhan, S. Wang, Y. Yuan, K. Jiao and S. Jiao, *Journal of the Electrochemical Society*, 2015, **162**, A1028.
28 J.-H. Lee, R. Black, G. Popov, E. Pomerantseva, F. Nan, G. A. Botton and L. F. Nazar, *Energy and Environmental Science*, 2012, **5**, 9558.
29 S. F. Lux, I. T. Lucas, E. Pollak and S. Passerini, *Electrochemistry Communications*, 2012, **14**, 47.
30 B. Ammundsen, D. J. Jones, J. Roziere and S. Passerini, *Chemistry of Materials*, 1995, **7**, 2151.
31 B. Ammundsen, P. B. Aitchison, G. R. Burns, D. J. Jones and J. Roziere, *Solid State Ionics*, 1997, **97**, 269.
32 A. Manthiram and W. Choi, *Electrochemistry and Solid State Letters*, 2007, **10**, A228.
33 J. C. Knight, S. Therese and A. Manthiram, *Journal of the Electrochemical Society*, 2015, **162**, A426.
34 E. A. Pomerantseva, T. L. Kulova, D. Zeng, A. M. Skundin, C. P. Grey, E. A. Goodilin and Y. D. Tretyakov, *Solid State Ionics*, 2010, **181**, 1002.
35 Y. Omomo, T. Sasaki and M. Watanabe, *Solid State Ionics*, 2002, **151**, 243.
36 W. Tang, H. Kanoh, K. Ooi and Y. Wang, *Journal of Materials Science Letters*, 2000, **19**, 1361.
37 S. Martinez, I. Sobrados, D. Tonti, J. M. Amarilla and J. Sanz, *Physical Chemistry and Chemical Physics*, 2014, **16**, 3282.
38 N. K. R. Palapati, E. Pomerantseva and A. Subramanian, *Nanoscale*, 2015, **7**, 3109.
39 A. Subramanian, N. S. Hudak, J. Y. Huang, Y. Zhan, J. Lou and J. P. Sullivan, *Nanotechnology*, 2014, **25**, 265402.
40 N. K. R. Palapati, A. Muth, Y. Zhu, C. Wang and A. Subramanian, *ASME Journal of Nanotechnology in Engineering and Medicine*, 2014, **5**, 021001.
41 J. E. Sader, J. W. M. Chon and P. Mulvaney, *Review of Scientific Instruments*, 1999, **70**, 3967.
42 C. Q. Chen, Y. Shi, Y. S. Zhang, J. Zhu and Y. J. Yan, *Physical Review Letters*, 2006, **96**, 075505.
43 R. Agrawal, B. Peng, E. E. Gdoutos and H. D. Espinosa, *Nano Letters*, 2008, **8**, 3668.
44 D. T. Tompsett and M. S. Islam, *Chemistry of Materials*, 2013, **25**, 2515.
45 J. B. Goodenough, *Journal of Applied Physics*, 1997, **81**, 5330.
46 Y. Paik, C. P. Grey, C. S. Johnson and J.-S. Kim, *Chemistry of Materials*, 2002, **14**, 5109.

Table of Contents Entry

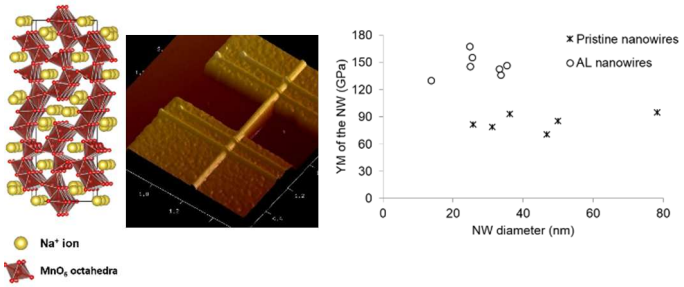

The Young's modulus of manganese oxide-based intercalation cathodes exhibits a strong correlation with the ionic content inside its structural tunnels.